F-Function Lobe Balancing for Sonic Boom Minimization

Brian Argrow,[1] Kurt Maute,[2] Geoffrey Dickinson[3]
Department of Aerospace Engineering Sciences
University of Colorado
Boulder, Colorado 80309

Charbel Farhat[1]
Department of Mechanical Engineering
Stanford University
Stanford, California 94305

Melike Nikbay-Bayraktar[4]
Instanbul Technical University
Istanbul, Turkey

1 ABSTRACT

F-function distributions for two-shock (bow and tail) signatures with minimum impulse, minimum overpressure, or minimum bow-shock overpressure were the culmination of the early sonic boom theory. Iterative methods were developed to derive cross-sectional area distributions for wing-body wind tunnel models to produce pressure signatures similar to the optimized predictions. A major shortcoming of these results is that they optimize the worst case—a two shock ground signature. Physically, the ground-signature parameter is minimized by maximizing the bow- and tail-shock strength as close to the aircraft as possible. This requires that intermediate shocks coalesce into the bow and tail shock as rapidly as possible. Less than optimal two-shock signatures result when this coalescence occurs closer to the ground. Also, the prescription of the *F*-function only determines a unique equivalent body of revolution, it does not produce a unique aircraft geometry, thus actual geometries are generally determined by trial-and-error. Sonic boom minimization research conducted at the University of Colorado as part of the DARPA Quiet Supersonic Platform, started in 2000, and follow-on work is reviewed. The aircraft shaping methods employ constrained optimization where certain design parameters such as total lift and the allowable excursions of the overall shape are constrained. The process starts with a realistic aircraft shape and ends with cross-section area and lift distributions to produce a tailored *F*-function that isolates some number of intermediate shocks. Flight test data from the

[1] Professor.
[2] Associate Professor.
[3] Graduate Student.
[4] Assistant Professor.

2003 Northrup Grumman tests of the F5-E and Shaped Sonic Boom Demonstrator are used for comparison.

2 *F*-Function-Based Vehicle Shape Optimization

Seebass and Argrow [1] discuss the origins of *F*-function-based vehicle shape optimization. Their discussion concludes with the Jones-Seebass-George-Darden (JSGD) theory that focused on tailoring the Whitham *F*-function that originated from Whitham's original paper [2]. During the first year of the DARPA Quiet Supersonic Platform (QSP) Project, the research group at the University of Colorado, Boulder (UCB) proposed and developed a vehicle shape optimization strategy for the minimization of the initial shock pressure rise (ISPR). The strategy went beyond the original JSGD theory to combine classical linear-theory based tools with state-of-the-art CFD tools. This work is described in Refs. 3-6.

2.1 The Lockheed Martin Point of Departure (POD) Aircraft

2.1.1 *F*-Function Lobe Balancing with Fuselage Optimization

The motivation for *F*-function lobe balancing is to preserve a multiple-shock ground signature, where "multiple-shock" refers to the presence of intermediate shocks between the bow and tail shocks. Argrow et al. [3] discuss the origin of the idea of lobe balancing and the two situations for which a multiple-shock signature is generated during high-altitude ($\geq$ 30 kft) cruise. The first case can occur for large aircraft where the ratio of the cruise altitude to the vehicle equivalent length is small enough that the midfield signature is frozen and an asymptotic N-wave overpressure signature does not form before intersecting the ground. The North American XB-70 Valkyrie is an example of an aircraft with a measured multiple-shock signature [3,7,8]. The second case is related to a feature of the *F*-function first discussed by Whitham [2] and later discussed in the context of sonic boom minimization by Koegler [9,10]. In this case, a negative-positive lobe pairing of equal magnitude will evolve into a shock wave that propagates into the far field without coalescing into other shocks. The Lockheed F-104 Starfighter is an example of a small aircraft that can produce a three-shock signature, even when cruising at high altitude [2,8]. Hayes and Haefeli [11] plot the F-104 *F*-function which shows a balanced lobe pair that produces an intermediate shock that does not merge with the bow or tail shocks. Argrow et al. also discuss how the F-104 experimental data verifies Whitham's predication that the intermediate shocks decay more rapidly than the bow and tail shocks as the aircraft altitude is increased.

Farhat et al. [4] present an *F*-function based vehicle shape-optimization scheme to minimize the ISPR. In Farhat et al. [5] the scheme is modified to seek negative-positive lobe pairs in the *F*-function then to directly modify the vehicle geometry to globally minimize the magnitude of the integrated area difference between negative-positive lobe pairs.

For the optimization scheme applied to the Lockheed Martin Point of Departure (POD) Aircraft, two parameters describe the inclination of the nose of the target aircraft and its curvature

intersection with the fuselage. The intersection between the fuselage and the nose is constrained to remain C^1 continuous. Six parameters control the dihedral, sweep, and twist angles of the canard and the wing; specifically, one vertical and one horizontal degree of freedom (dof). The vertical dofs are allowed to move independently, but the horizontal dofs of the canard are constrained to have the same motion, and the horizontal dofs of the wing are also constrained to have the same motion.

In each case, the vehicle length, lift (weight), and inviscid drag (induced and wave drag) are constrained to remain constant. Figure 1 (a)-(c), from Farhat et al. [4], shows surface pressure contours for the unmodified POD, a shape-optimized version without lobe balancing, and a shaped-optimized version with lobe balancing. For the cases shown, the cruise weight is 98,000 lb, at an altitude of 45,000 ft, and a Mach number of 1.5. The cruise angle of attack (determined by matching lift to the vehicle weight), is 0.7°. Results for cruise Mach number of 2.0 are reported in Table 2. The primary shape changes are with the canard and the wing dihedral. This is partly due to limits placed on the shape parameters while satisfying fixed constraints. Geometry limits are required to maintain a reasonable aerodynamic shape; according to linear theory an unconstrained geometry will approach a needle shape to minimize the thickness ratio. Details of the parameter choices and constraints are discussed in Farhat et al. [4].

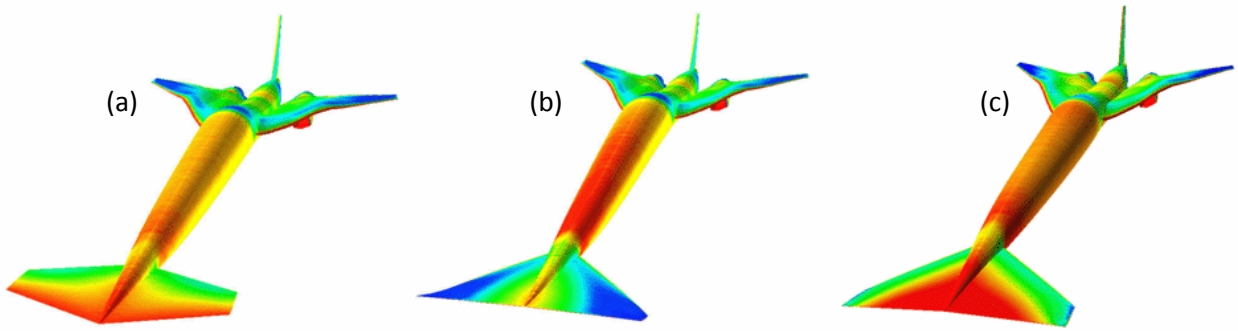

Figure 1 Lockheed Martin POD pressure contours at cruise condition: (a) unmodified airframe, (b) shape-optimized without lobe balancing, and (c) shape-optimized with lobe balancing.

An *F*-function comparison of the original POD to the lobe-balanced optimized version is shown in Figure 2. Note the difference caused by the shape and lift change of the canard. The shift and magnitude increase of the *F*-function near the nose is consistent with the JSGD result that nose bluntness reduces the ISPR. According to JSGD theory, an infinitely blunt nose minimizes ISPR by maximizing the shock strength as close to the aircraft as possible so that atmospheric attenuation is maximized [1, 12, 13]. Note that in Figure 1 the optimization morphs the canard such that the maximum amount of canard volume and lift are moved as far forward as possible. Since lift is directly proportional to cross sectional area of the equivalent body of revolution, the lift at the nose adds to the volumetric bluntness. There is also a noticeable rearward shift and reshaping of the wing contribution approximately between $0.65 < y/L < 0.9$.

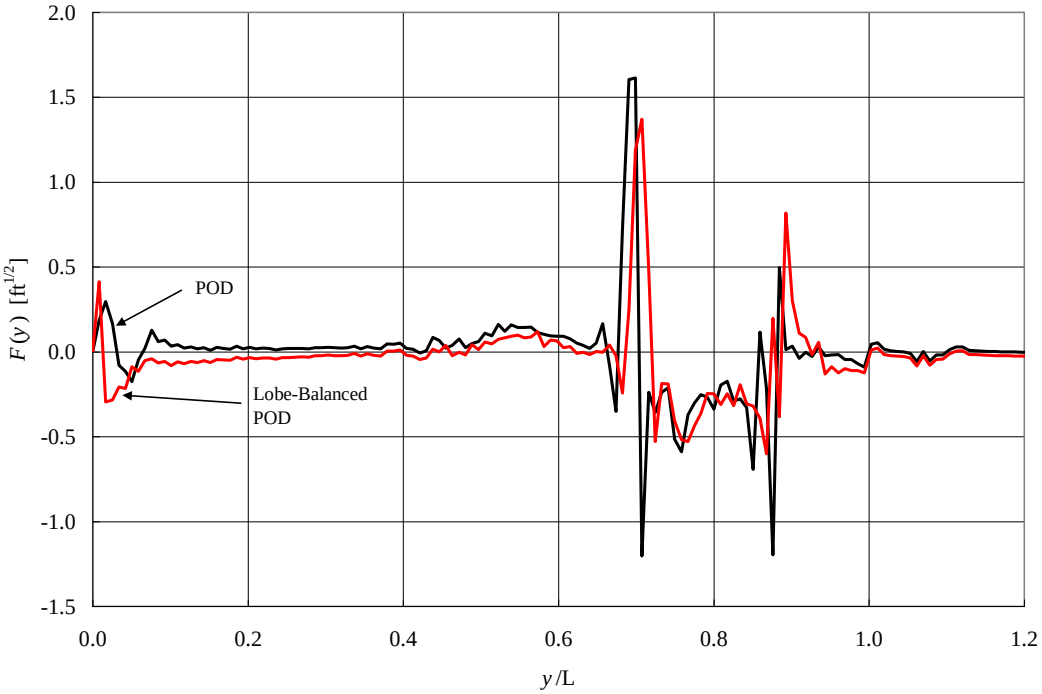

Figure 2 *F*-functions vs. normalized distance for the POD and lobe-balanced optimized POD.

Table 1 and Table 2, from Farhat et al. [4] report the optimization results for the POD for cruise Mach numbers of 1.5 and 2.0. The first column indicates whether *F*-function lobe balancing was, or was not, used. The second column indicates the number of optimization iterations for convergence. In the third column, the ISPR of the original POD is indicated in parentheses, followed by the optimized results, both reported in units of lb/ft^2 (psf).

Table 1 Shape Optimization of the POD for $M_\infty = 1.5$

Shape Optimization	Iterations	(Initial) Optimized ISPR [psf]
Without Lobe Balancing	13	(1.616) 0.152
With Lobe Balancing	9	(1.616) 0.083

Table 2 Shape Optimization of the POD for $M_\infty = 2.0$

Shape Optimization	Iterations	(Initial) Optimized ISPR [psf]
Without Lobe Balancing	15	(1.866) 0.328
With Lobe Balancing	12	(1.866) 0.324

F-functions for the M_∞ = 1.5 case were input into the ARAP [11] atmosphere propagation code to compute ground signatures for the unmodified and lobe-balanced optimized POD shown in Figure 3. For the lobe-balanced case the intermediate shock is still relatively strong and the tail shock is basically unchanged. Note that for a ground observer, the time between the bow and intermediate shock is about 28 ms. This exceeds the minimum interval of about 20 ms for which the human ear can distinguish separate acoustic events [1].

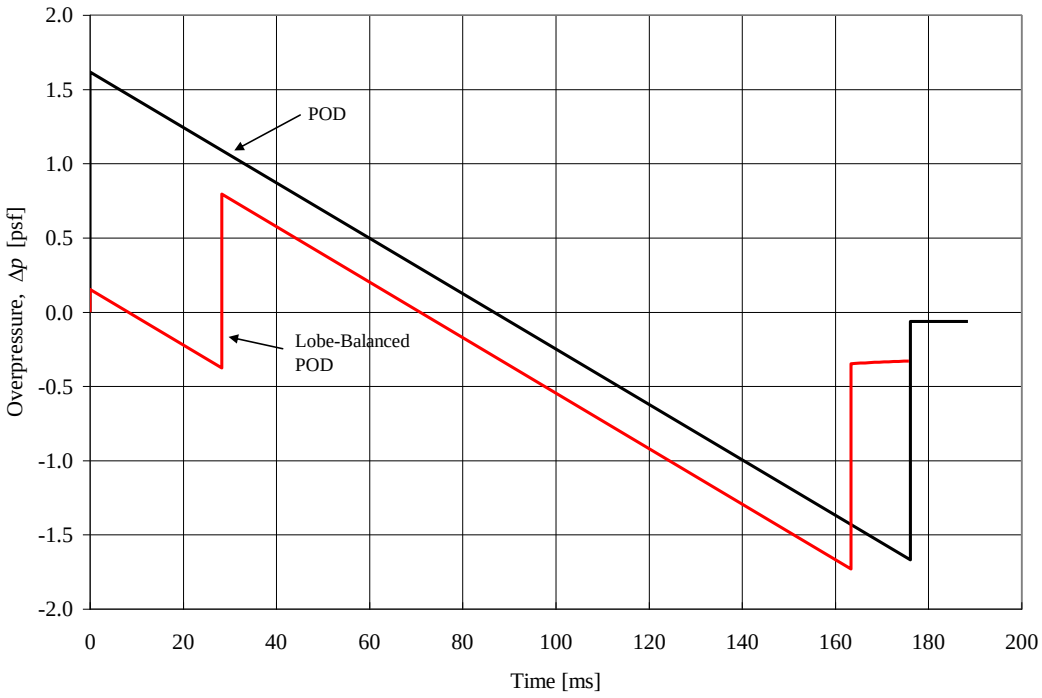

Figure 3 Ground signatures for the POD and the lobe-balanced optimized POD computed using ARAP.

2.1.2 Propulsion Effects on ISPR

In a review of sonic boom theory, Hayes [14] stated that a supersonic aircraft appears to a distant observer as a linear source distribution whose strength is determined by three terms: a term proportional to the lift, a term proportional to the difference between the cross-sectional area of the engine exhaust and intake streams far from the aircraft, and a term proportional to the density decrease caused by heating from the shock system. At the same conference, Ferri [15] stated that the engine can be used to reduce the sonic boom and that the effects of the propulsion system are dependent on the engine cycle and flight Mach number. In neither case was there a detailed analysis or reference to experimental data to substantiate these comments.

Ressler [16] derived equations to estimate the effect of engine cycle and efficiency on the equivalent body. He modeled a turbofan engine as an ideal, isentropic ducted fan with an ideal turbine power pod; however there is ambiguity in the system definitions. With the assumption that the area decrease generated by the fan must be larger than the increase caused by the turbine,

Ressler derives an equation that gives a lower bound for overall engine efficiency. Seebass [16] stated that the effects of exhaust pluming, as proposed by Ressler, "…would only reduce the boom due to lift by about five percent (assuming this is accomplished without additional wave drag—which it cannot be)."

Miller and Carlson [18] showed that the use of heat and/or force fields can lead to finite-rise-time pressure signatures. They also show that the energy required to operate these schemes is roughly twice what is required to maintain steady level flight. Their analysis also assumed no added weight for the field generating equipment. Miller [19] extended this work to examine thermal fins applied to a proposed 300-ft SST. He showed that by burning fuel as the heat source in *80-ft* fins, under the nose and above the tail, the modified SST would produce a finite-rise-time signature in place of both the bow and tail shocks. He estimates that this system would require 60% more fuel. However, his analysis does not include the weight added, or the effects on performance, due to this system. He concludes that this system could be feasible.

Swigart [20] experimentally verified the concept of a heat field used to reduce the sonic boom. Using fins approximately one-third to one-half the aircraft length, extended below a wind tunnel model, he showed that the sonic boom can be reduced. He also showed that off-axis structure can be use to produce finite-rise-time signatures and he proposed that off-axis combustion might be advantageous from a sonic boom standpoint.

The DARPA QSP program generated renewed interest in energy deposition for sonic boom minimization. Shneider et al. [21] discuss some of computational and experimental work done at Princeton as part of the DARPA QSP program. They focused on reducing the strength of the bow shock with upstream energy deposition. While they show some reduction in the bow shock strength, they indicate that their results are preliminary. Marconi et al. [22] present a numerical investigation of the keel concept examined by Swigart [20] and report that the power requirement results are consistent with Refs. [18] and [19].

In the following section, a simple analysis is presented to investigate how engine exhaust might be used to modify the sonic boom signature for the POD aircraft.

2.1.3 Exhaust Plume Effects on the Equivalent Body and ISPR

The influence coefficient method for computing a quasi-one-dimensional flow is employed to model the evolution of the engine exhaust plume [23]. The algorithm was validated by comparing to examples in Zucrow and Hoffman [23] and Miller and Carlson [18].

Figure 4 illustrates the equivalent body of revolution, with various contributing components, for the POD aircraft as it would appear to an observer directly below the flight path. Cruise conditions for this and subsequent calculations in this section are M_∞ = 1.5 at an altitude of 45,000 ft with a vehicle weight of 98,000 lb. In Figure 4(a) the equivalent body includes contributions from the cross-sectional area and lift; this equivalent body is the lighter-colored cylindrical shape superimposed onto the silhouette of half of the POD. Note that the equivalent body is computed for the entire vehicle although, for clarity, only half the vehicle is shown. The

exhaust plume is added as an extension from the rearmost portion of the POD fuselage, appearing as a small flair emerging beneath the vertical tail.

No information for the proposed engine for the POD was provided to the authors by Lockheed Martin. After surveying representative engine choices based on those currently available, the Pratt & Whitney F-100, low-bypass, mixed exhaust turbofan engine was chosen for the following analysis. Data for this engine was taken from Mattingly et al. [25]:

Exhaust stagnation temperature T_{0e} = 1681 K (non afterburning)

Exit Mach number M_e = 2.214

Nozzle exit area A_e = 1.12 m^2

The nozzle is assumed to be perfectly expanded such that the exit pressure is equal to the ambient pressure. The engine mass flow rate was computed with the assumption of no inlet spillage and the ratio of specific heats for the exhaust was set to γ = 1.4.

In Figure 4(b) and (c) the equivalent body includes the contribution from the exhaust plume assumed to start at the axial location of the exit of the engine nacelle. The annular region, downstream of the bulge generated by lift from the wing, is the difference in cross-sectional area from inclusion of the plume area. The cross-sectional area downstream of the introduction of the plume is reduced from that indicated by the inner radius of the annular region.

Figure 4 (a) View of the Lockheed Martin POD with the equivalent body due to cross-sectional area superimposed and a simulated plume extending from fuselage rear; (b) equivalent body including cross-sectional area, lift, and exhaust plume located at the *x*-coordinate of the engine exhaust nozzle; (c) equivalent body from (b) superimposed on the oblique POD view.

Figure 5 shows the effect on the ISPR by the starting location of the plume. As the plume is moved from the nose of the aircraft, it first causes a slight ISPR increase, followed by a much larger decrease. Beyond about x = 29 m the plume no longer directly affects the ISPR. This indicates the F-function balance point beyond which F-function contributions cannot feed into the bow shock. The balance point y_0 is the point along the y-axis where the integral $\int_0^y F(\xi)d\xi$ has maximum positive value [3-5]. Of course it is unlikely that an exhaust plume would originate at the nose of the aircraft; however, the plot in Figure 4 (a) View of the Lockheed Martin POD with the equivalent body due to cross-sectional area superimposed and a simulated plume extending from fuselage rear; (b) equivalent body including cross-sectional area, lift, and exhaust plume located at the *x*-coordinate of the engine exhaust nozzle; (c) equivalent body from (b) superimposed on the oblique POD view.

Figure 5 was created to compare to results reported from Refs. [18-22], discussed in the previous section. The purpose of this exercise is to show the small influence of the plume and to show how the plume influence on the ISPR diminishes as it approaches the balance point. Note that regardless of the location of the plume, it affects the overall location of the balance point,

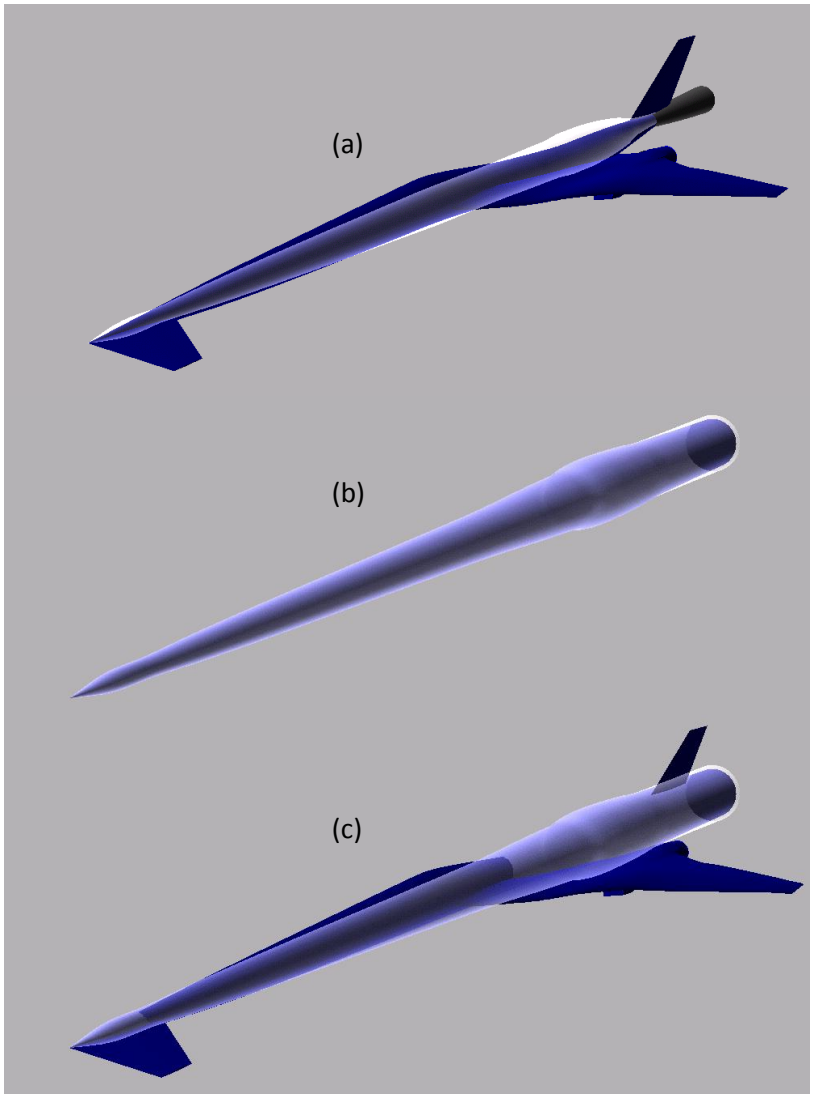

depending upon how it subtracts or adds to the equivalent body.

Figure 4 (a) View of the Lockheed Martin POD with the equivalent body due to cross-sectional area superimposed and a simulated plume extending from fuselage rear; (b) equivalent body including cross-sectional area, lift, and exhaust plume located at the *x*-coordinate of the engine exhaust nozzle; (c) equivalent body from (b) superimposed on the oblique POD view.

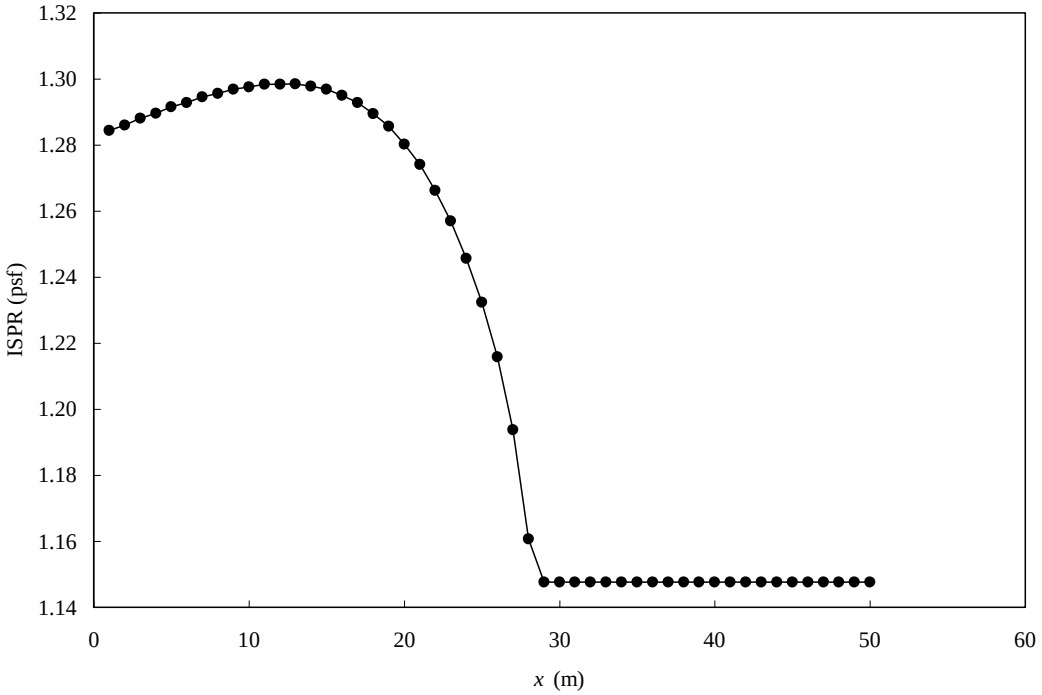

Figure 5 Effect of plume location on ISPR for the POD.

3 Shaped Sonic Boom Demonstrator (SSBD)

3.1 F5-E and SSBD Results

Pawlowski et al. [26] provide an overview of the Shaped Sonic Boom Demonstrator (SSBD) program, describing its objective to be the first aircraft designed to produce a specific ground overpressure signature. Figure 6 shows the F5-E and SSBD CAD models showing the F5-E nose modification used to create the SSBD variant. For the Euler calculations that follow, the final computational mesh for the F5-E contained 198,6319 elements and 389,569 nodes, while the SSBD mesh contained 2,121,227 elements and 417,017 nodes. The models were run for conditions similar to those reported for the SSBD tests, flight Mach number of 1.34, with ambient conditions from the 1976 US standard atmosphere at 32 kft.

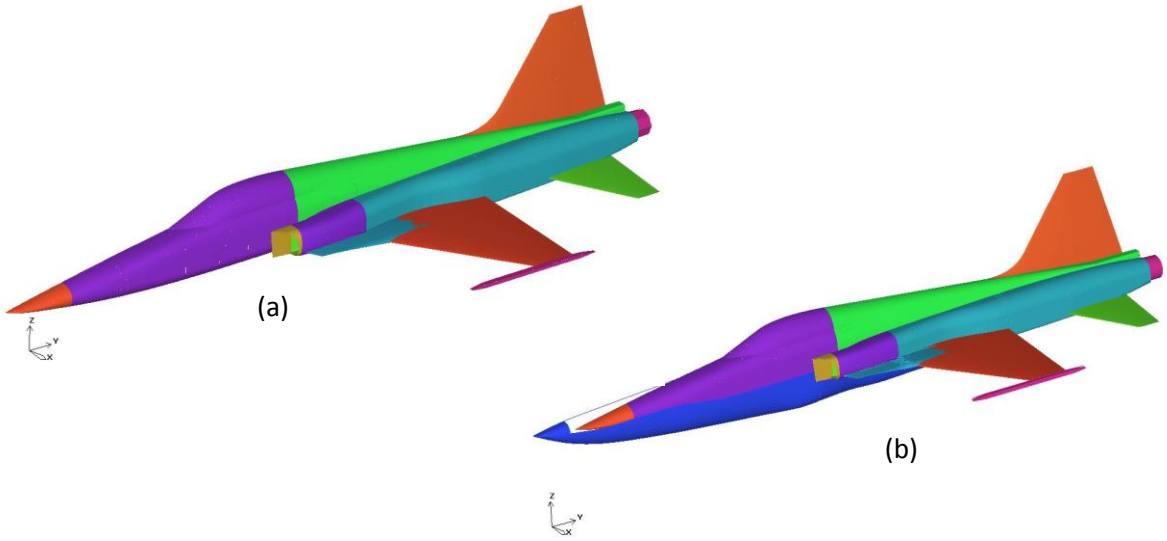

Figure 6 CAD models of, (a) the Northrup Grumman F5-E and, (b) the SSBD.

In Figure 7 the *F*-functions *F*(*y*) for the F5-E and SSBD are compared. Here, $y = x - \beta r$ is the characteristic distance with (*x*,*r*) the axial and radial coordinates, respectively, and $\beta = \sqrt{M_\infty^2 - 1}$. Note that the SSBD is about 1.5-m longer than the F5-E, so that in Figure 7 the SSBD *F*(*y*) starts further to the left. At the nose the magnitude of *F*(*y*) for the SSBD is much larger than for the F5-E, corresponding to an effectively blunter nose. As discussed earlier, this is a feature of a bow shock minimized according to JSGD theory. Following this, the most noticeable difference is for *y*-values 1-8 meters from the nose where the SSBD profile is noticeably flatter than the F5-E with more negative area in this region. Such shape of *F*(*y*) should produce a "flattop signature" [1, 12, 13].

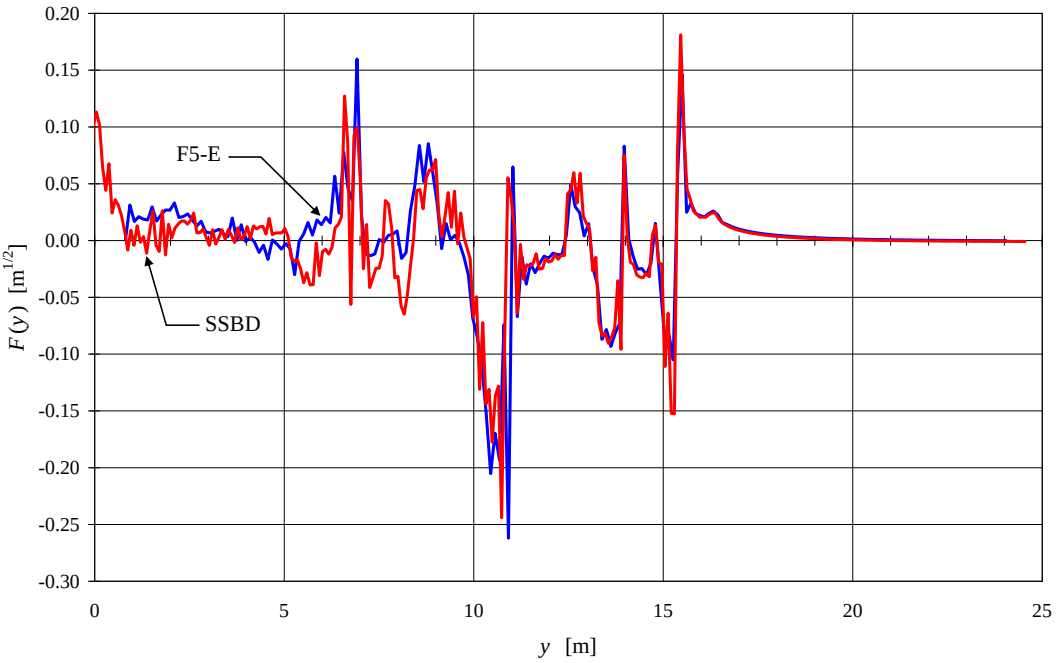

Figure 7 *F*-function comparison of F5-E and SSBD.

Figure 8 shows the measured ground overpressure signatures from the F5-E and SSBD flight tests and Figure 9 is an overlay of the ground signatures computed with the area "slicing tool" and the ARAP propagation code used in the UCB aircraft shaping codes [3-6]. The slicing tool builds the equivalent body of revolution by cutting planes through the aircraft geometry, inclined at the freestream Mach number and including the equivalent area contribution from lift as described in Ref. [27]. The agreement is relatively good in overpressure magnitudes and signal duration, and the computation clearly predicts the N-wave for the F5-E and the flattop signature observed for the SSBD. For this comparison, the ARAP overpressure vs. distance output was converted to overpressure vs. time using the cruise Mach number of 1.34 and the local speed of sound of 986 ft/s (standard atmosphere model).

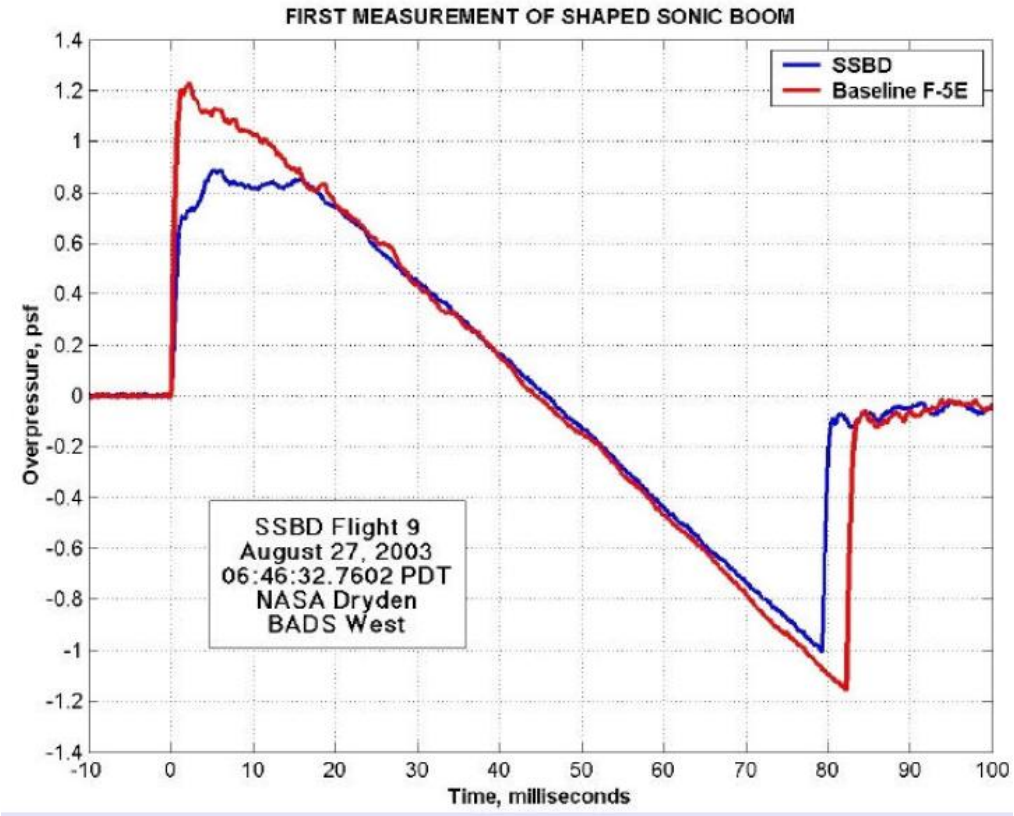

Figure 8 Ground signatures from the SSBD tests (plot provided by Northrup Grumman, 2005).

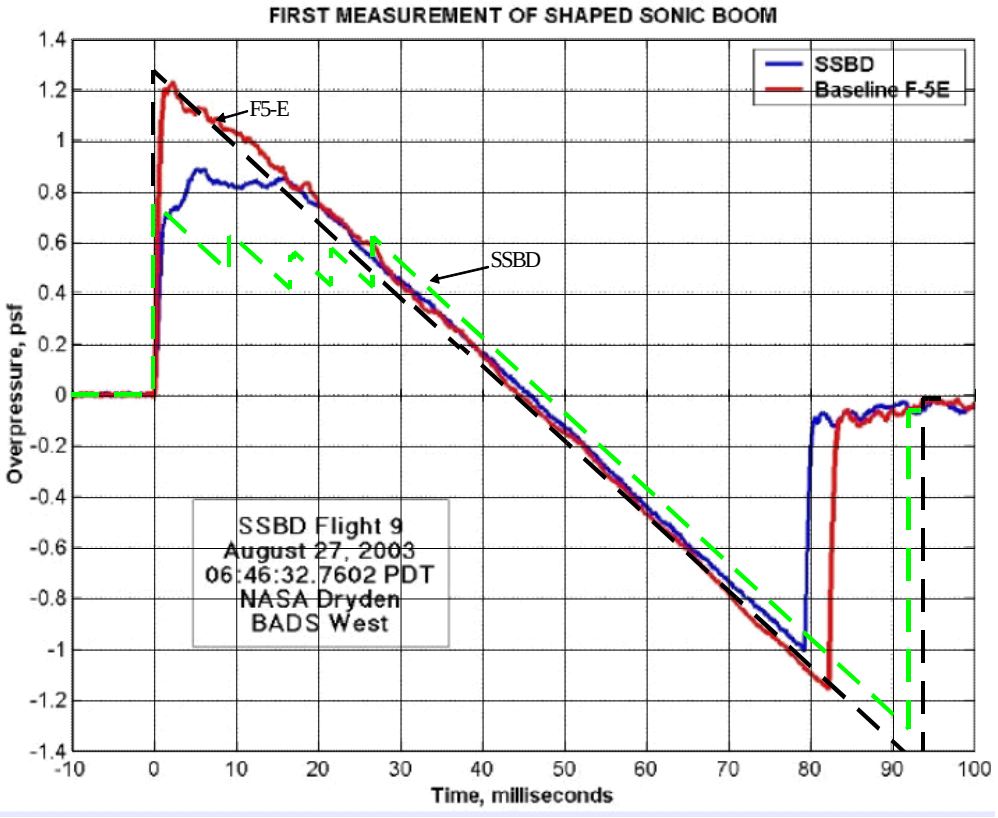

Figure 9 Computed F-5E and SSBD signatures overlaid onto experimental data.

Much can be determined about the origins of the observable features in the ground signatures using the linear-theory-based tools. Figure 10 and Figure 11 were created to determine how the aircraft shape affects the *F*-function and near-field pressure distributions. Figure 10 shows a side view of the F5-E and the SSBD, similarly Figure 11 shows planform views. The airframe silhouettes are plots of the (X,Y) coordinates where the area slicing routine cuts through the vehicles and projects surface coordinates onto the vertical plane of symmetry and a horizontal plane that contains the X-axis of the CAD model. The slicing angle, the sum of the freestream Mach angle and the vehicle angle of attack, is most evident in Figure 10 (a). The equivalent body cross-sectional area distribution $A(y)$, $F(y)$, and near-field overpressure at 10 m from the equivalent body $p(y)$ are plotted along the axis to the right. Again, it is obvious that the SSBD is a bit longer than the F5-E. The next feature to notice is that the dip in $A(y)$, between the maximum canopy height and the engine inlet, is smaller for the SSBD than for the F5-E, so there is improved 'area ruling'. The remainder of the $A(y)$ distributions are quite similar.

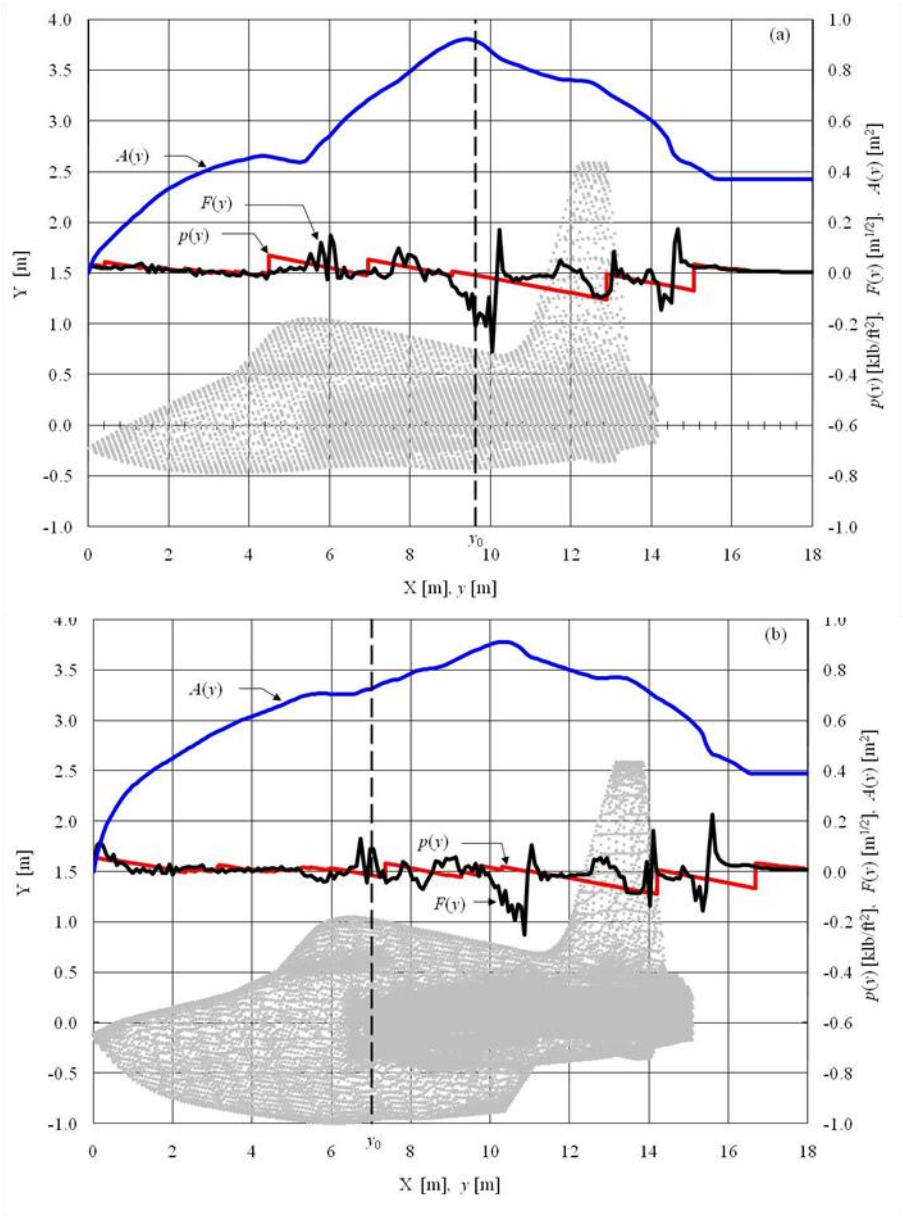

Figure 10 Equivalent body area distributions $A(y)$, F-function $F(y)$, and overpressure $p(y)$, at 10 m from the equivalent body, and balance point y_0 with side view, (a) F-5E, (b) SSBD.

Figure 11 shows a planform view of both aircraft. The canopy and inlet shocks are easily visible in the near-field pressure distribution. Note that the shaping of the SSBD seems to almost eliminate the canopy shock. The inlet shock appears to be of about the same magnitude for both aircraft. Evidently, the origin of the canopy shocks can be traced to the positive $F(y)$ pulses at about y = 6 m and y = 7 m for the F5-E and SSBD, respectively. The origin of the inlet shock can also be traced to about y = 8 m and y = 9 m respectively. The expansion-compression of the wing is obvious in the $F(y)$ plot near y = 10 m and y = 11 m, respectively.

The most important observation is the movement of the balance point y_0. This is the point along the y-axis where the integral $\int_0^y F(\xi)d\xi$ has maximum positive value [3-5]. For a two-shock signature all shocks ahead of y_0 feed upstream and eventually coalesce with the bow shock and shocks downstream of y_0 eventually merge with the tail shock to produce an N-wave. Reshaping the F5-E into the SSBD moves the y_0 a few meters upstream. More importantly, y_0 is moved ahead of the inlet shock on the SSBD. This means that the inlet shock does not feed into the bow shock and although the canopy shock still feeds into the bow shock, the magnitude of the canopy shock is greatly reduced for the SSBD.

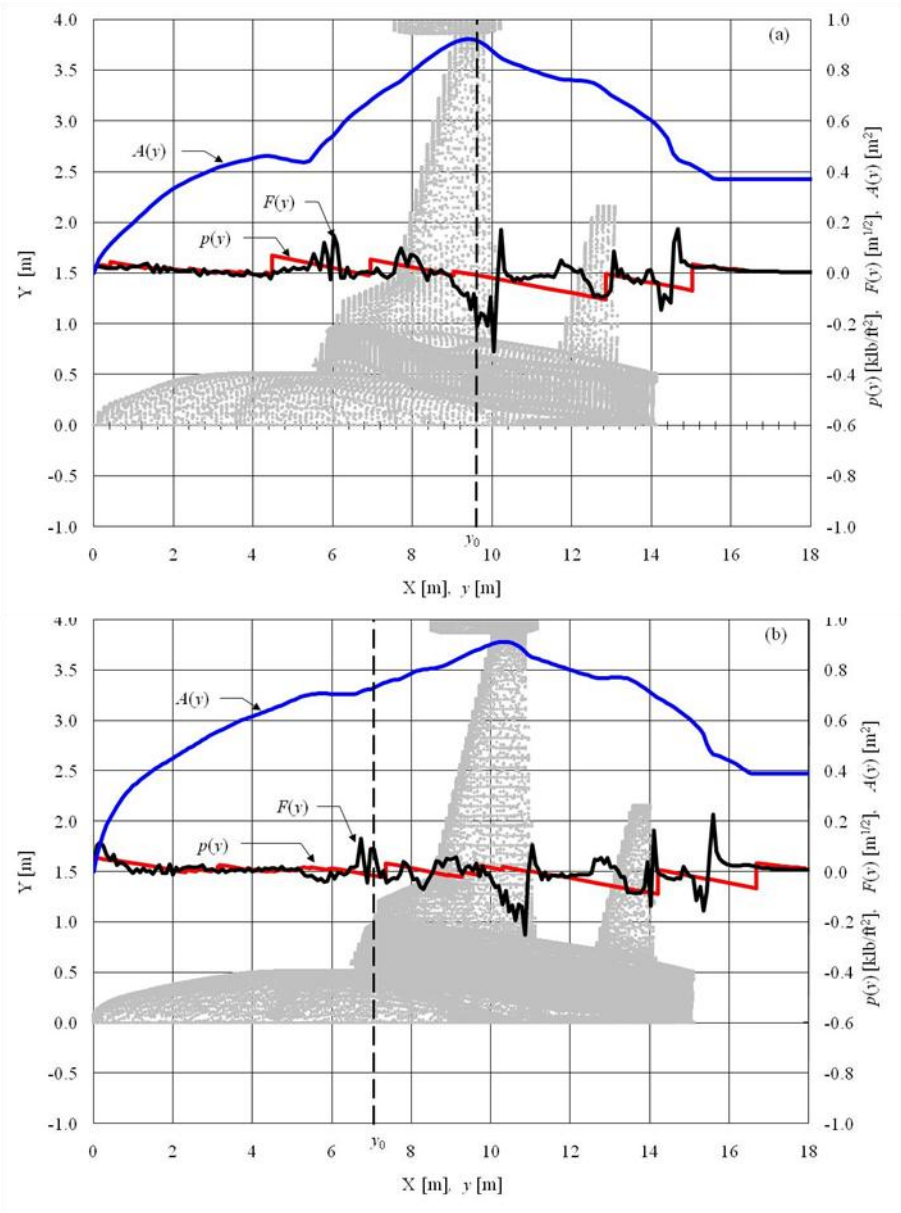

Figure 11 Equivalent body area distributions $A(y)$, F-function $F(y)$, and overpressure $p(y)$, at 10 m from the equivalent body, and balance point y_0 with planform view, (a) F-5E, (b) SSBD.

The linear-theory-based analysis shows, in simple graphical terms, how the SSBD modifications favorably altered the wave field by reducing or eliminating the contribution to the ISPR from both the canopy and inlet shocks.

3.2 Optimization Results for the F-5E and SSBD

Some recent optimization results for the F-5E and SSBD from Maute et al. [6] are now presented. A finite-volume approximation of a steady-state Euler flow is used to compute the near-field pressure about the aircraft and linear acoustic methods for predicting the initial shock pressure rise at the ground. The two methods used in previous UCB work to compute the ground pressure signature are compared. The first (MCL) uses McLean's formula [28] to estimate the ground signature,

$$\Delta p = \frac{2^{5/4}}{z^{3/4}} \frac{\gamma}{\sqrt{\gamma+1}} \left(M_\infty^2 - 1\right)^{1/8} \sqrt{p_a p_g \int_0^{y_0} F(x)dx}$$

where z is the flight altitude, γ is the ratio of specific heats, p_a is the ambient pressure at altitude, and p_g is the atmospheric pressure on the ground. The second method uses the ARAP [11] code that uses linear acoustics to compute the propagation of the pressure signal from the vicinity of the aircraft to the ground. Both methods are compared to the F-5E and SSBD flight tests results from the previous section.

To reduce the sonic boom, an adjoint optimization method is employed which allows for the manipulation of the ground signature by varying the shape of the aircraft while considering constraints on the aerodynamic performance, such as drag, lift, and aerodynamic moments. Two approaches for altering the shape are compared: a CAD-based (CB) approach and a technique directly operating on the triangulation of the surface in the computational mesh (CF). Optimization results are generated with manipulation of the nose section shape of the F5-E to examine the influence of the sonic boom prediction method and shape variation techniques on the optimal design. Details of the adjoint sensitivity analysis are presented in Maute et al. [6].

Figure 12 shows the portion nose section of the F5-E that was manipulated during the optimization process.

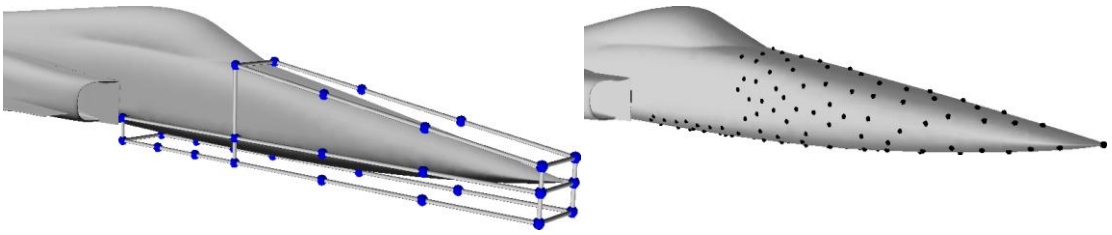

Figure 12 Portion of the F-5E nose modified during optimization.

Results from Maute et al. [6] are presented in Figure 13 and Figure 14. A comparison of the images shows a distinct difference in the shape of the vehicle nose between the CB and CF approaches. In the Figure 13 CB case, the nose tip has a very distinct upward curvature, while the CF case in Figure 14 shows a general rippling of the nose, similar to wind tunnel images from an alternating compression-expansion scheme investigated by Runyan and Henderson [29]. Figure 15 is close-up of the nose for the MCL CF case and shows that the nose has swelled into a bulbous, blunt shape. The images and corresponding $F(y)$ plots repeat the trend shown earlier for the optimization of the POD. In all cases, the converged vehicle shape maximizes the bluntness of the equivalent body at the nose; this includes the contributions from volume and from lift. In the case of the POD, this meant that the canard moved as much lift and volume forward as was allowed under the geometric constraints. For the CB cases, the nose of the vehicle is turned upward, relative to the incident wind, to create an angle of attack for lift, and in the CF cases, the nose became bulbous with rippling of the remaining nose surface that generates alternate expansions and compressions. Finally, Figure 16 shows the ground signatures of the optimized F5-E cases compared to the original F5- E and SSBD. With the exception of the RTM CF case, the manipulations of the nose reduced the ISPR of the optimized cases below that of the SSBD. Of course this reduction in ISPR is not without penalty, since it is obvious that the shaping results in much higher drag (drag calculation not reported here).

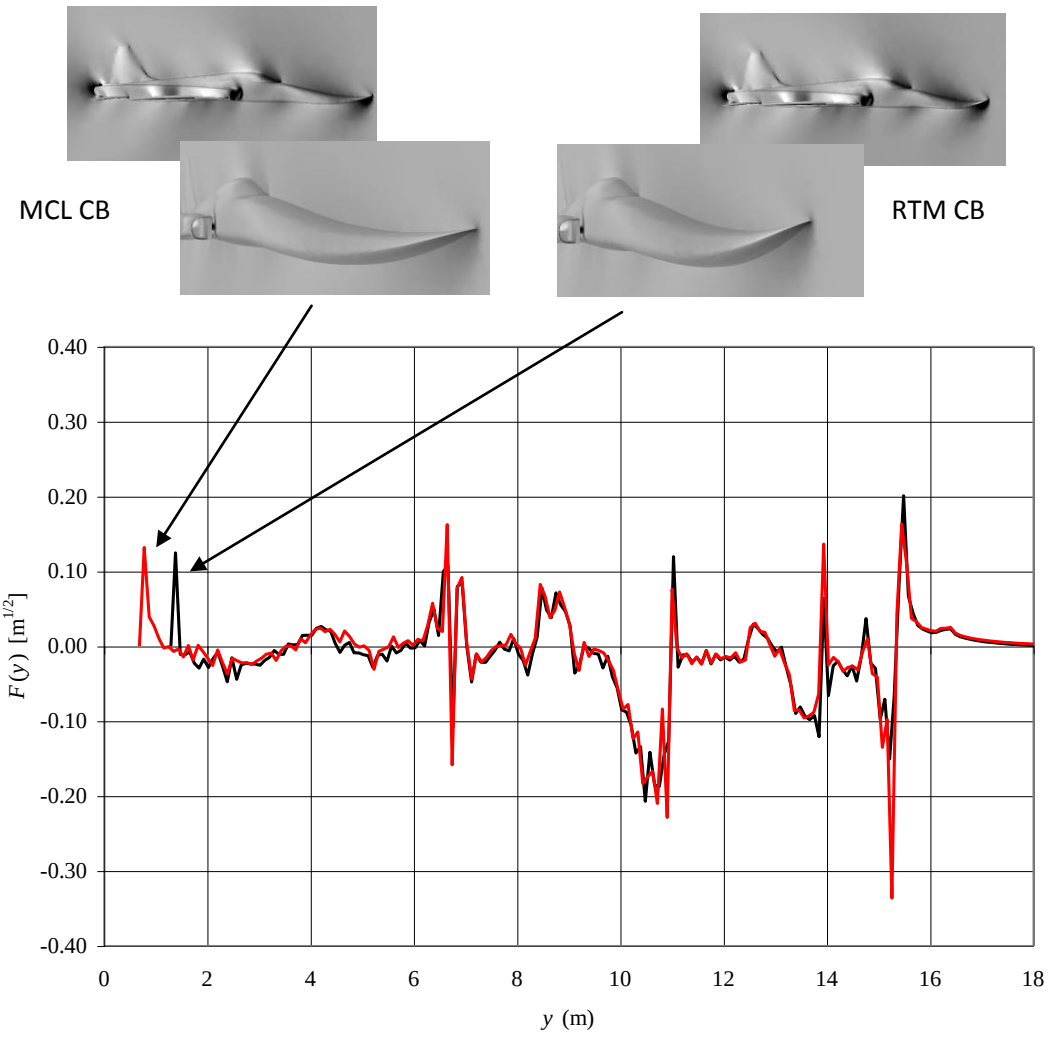

Figure 13 CAD-based optimization results using the McLean formulation (MCL CB) and ray-tracing method (RTM CB) for the F5-E. Plot shows the $F(y)$ plotted along the aircraft centerline.

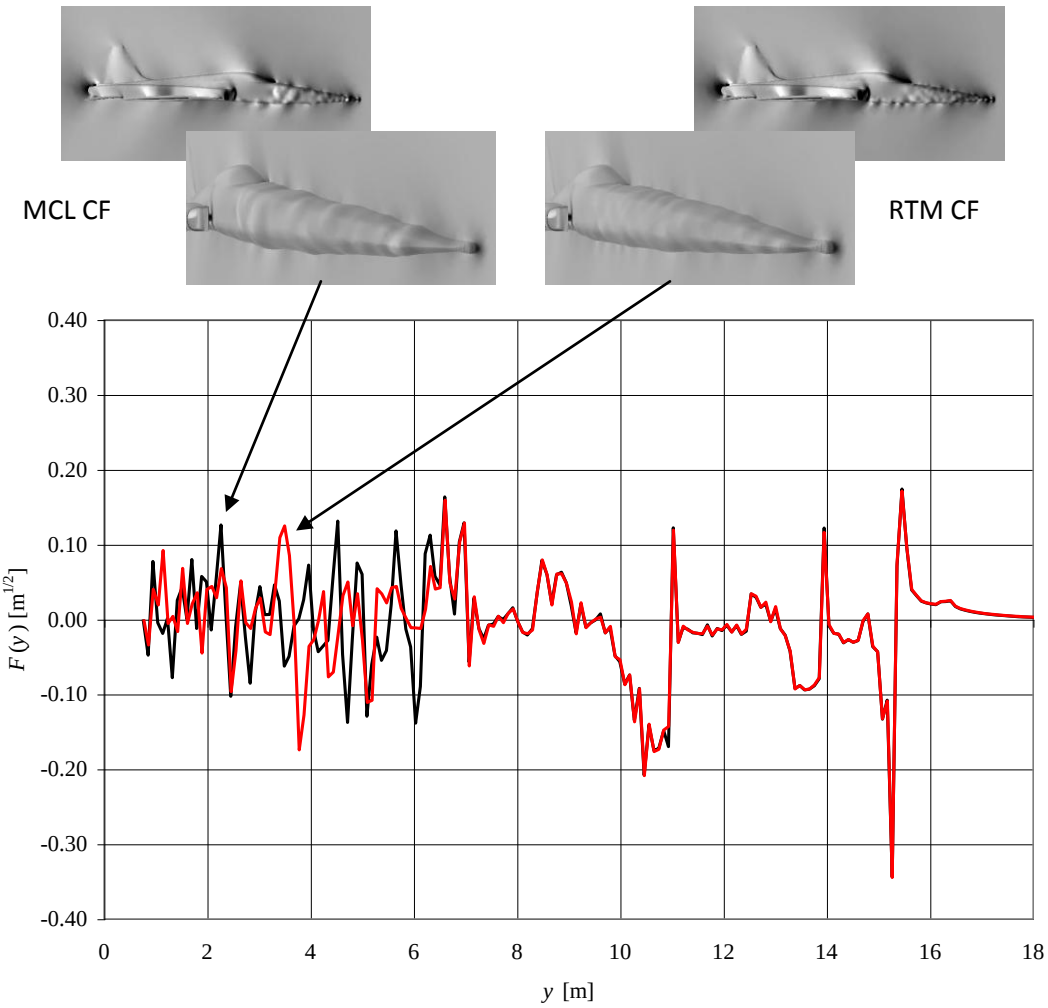

Figure 14 CAD-free optimization results using the McLean formulation (MCL CF) and ray-tracing method (RTM CF) for the F5-E. Plot shows the $F(y)$ plotted along the aircraft centerline.

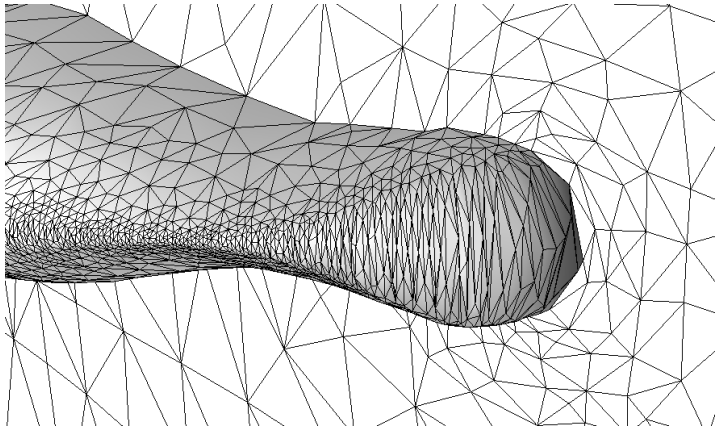

Figure 15 Close-up of the MCL CF case.

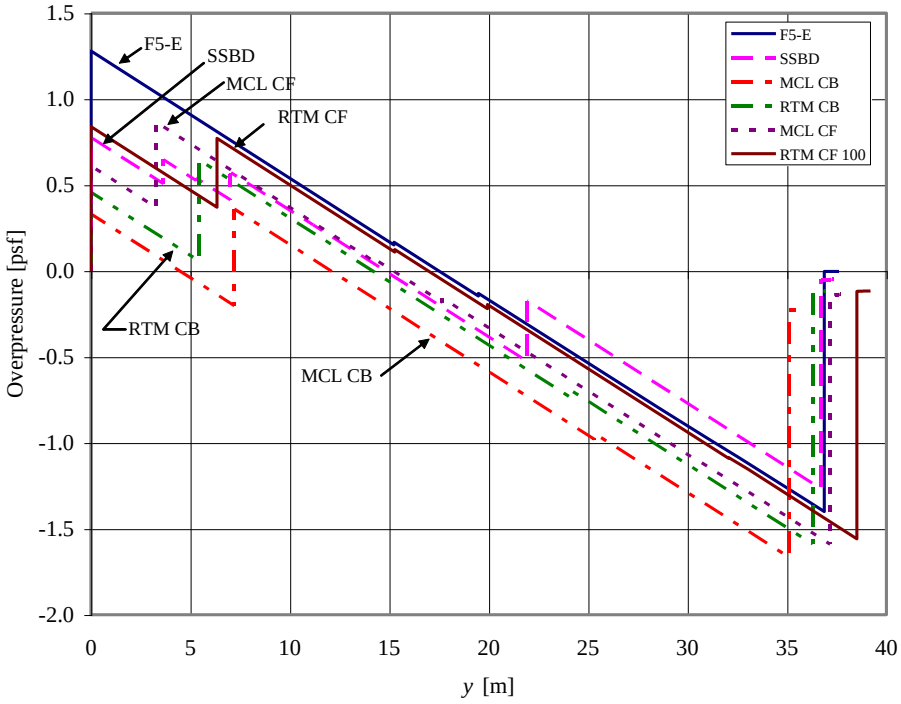

Figure 16 Ground overpressure signature comparison of the optimized F5-E cases compared to the unmodified F5-E and the SSBD.

4 Improved Lobe Balancing Strategy

The optimization routine, presented in Sect. 3, focused on an automatic, global balancing of *F*-function lobes. An improved strategy should allow the designer to focus on the strongest intermediate shocks and allow constrained redistribution of equivalent area, with some combination of actual aircraft volume and the equivalent area from lift. The redistribution must be constrained so that the new geometry meets requirements for trimmed, level flight.

As a first step, simple "clean" geometries, such as those investigated in earlier works, e.g. [30-33], will be investigated. Two representative geometries are shown in Figure 17. In both cases, the volume of the fuselage, wing, and engine nacelles, and the wing lift distribution can all be written in simple forms, for relatively simple computations of $F(y)$. Investigation of these simple geometries will enable the development of a strategy to tune the current lobe-balancing scheme to focus on the isolation of the strongest intermediate shocks that eventually coalesce and contribute to the bow and tail shock overpressures.

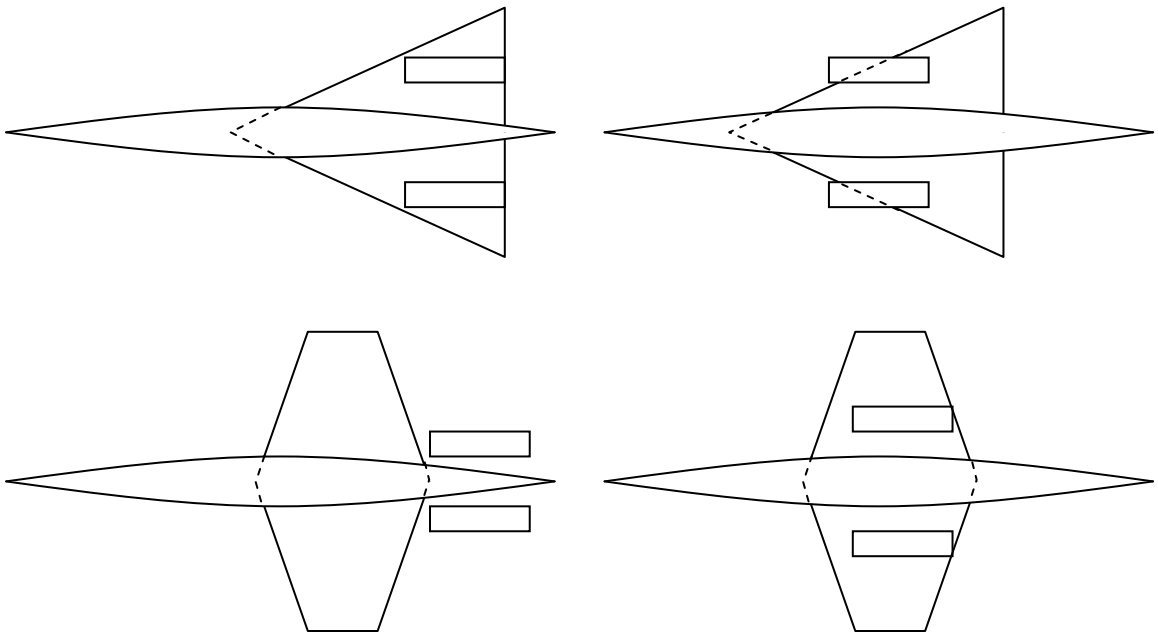

Figure 17 Simple geometries to study F-function lobe balancing. Shows how components can be easily moved to change the configuration.

Gottlieb and Ritzel [34] reviewed the *F*-function formulations in Whitham [2] that includes the formulation of M. J. Lighthill for non-smooth bodies. Gottlieb and Ritzel's discussion provides the most thorough assessment of *F*-function formulations and they give guidelines for the appropriate use of these formulations. They also point out that the most appropriate *F*-function for mid-field calculations supersonic aircraft has generally not been used. The calculations for the proposed lobe-balancing study will employ the appropriate *F*-function as prescribed by Gottlieb and Ritzel.

5 Summary and Conclusions

A review of the sonic boom minimization work at the University of Colorado, Boulder for the DARPA QSP program was presented. New work to advance the state-of-the-art for supersonic aircraft shaping technologies that was completed after the QSP program was also presented, with a brief proposal for future work. Several aspects of linear-theory-based optimization and related topics were investigated. In addition, the Northrup Grumman SSBD team provided CAD models and experimental results from the SSBD experiments conducted in 2003. This gave the UCB group an opportunity to validate the aircraft area slicing routine and ARAP propagation routines incorporated into the UCB aircraft-shaping code.

The UCB *F*-function lobe-balancing shape optimization was applied to the POD vehicle. In each case, the optimized vehicle shape produced a multiple shock signature (three shocks). Shape optimization without lobe balancing was also reported to illustrate the additional ISPR reduction for the *F*-function lobe-balanced airframe. ISPR values were reduced from 1.616 psf to 0.083 psf for Mach 1.5 cruise and 1.866 psf to 0.324 for Mach 2.0 cruise. These results show an ISPR

reduction by a factor of 20 and 6, respectively and compare favorably to the original DARPA QSP goal of 0.3 psf.

A quasi-one-dimensional exhaust plume model was incorporated into the airframe optimization to examine how much the exhaust plume might affect the equivalent body of revolution and the ISPR. For the POD airframe, inclusion of the exhaust plume had minimal impact on the body of revolution. When the origin of the plume was located at the exit plane of the engine nacelles, it caused a reduction in the cross-sectional area of the equivalent body of revolution. As required, this reduction is persistent, thus directly reduces the cross-sectional area due to lift that persists downstream of the airframe. When the origin of the plume is arbitrarily moved from the nose of the POD airframe, it first causes a slight increase in the ISPR, then a more substantial decrease until the origin of the plume passes downstream of the balance point, after which it does not influence the ISPR. Propulsion effects are minimal overall, but might be useful in a global optimization scheme that involves mitigation of the tail shock.

As discussed in Argrow et al. [3] and Farhat et al. [4], early linear-theory based optimization schemes that culminated in the JSGD theory [1] optimize the 'worst case' boom signature—a two shock signature. In these references we develop the hypothesis that for a vehicle of constrained length and weight at fixed cruise conditions, optimization of the sonic boom requires a multiple (more than two) shock signature. The POD optimization results support this hypothesis. In each optimization case, the solution converged to a multiple (three) shock signature. The geometric parameters during the optimization search are limited to eight, and somewhat arbitrary limits were placed on the excursions of these parameters. If the geometry of the target vehicle were less constrained by increasing the number of optimization parameters and increasing their excursion limits, the optimization result might contain more non-coalescing intermediate shocks. While the results are not a hard proof, they certainly provide evidence for a multiple-shock requirement. More cases with different initial geometries are required.

The analysis of the F5E and SSBD airframes are further validation of a linear-theory-based approach. While guided by linear-theory principles, the Northrup Grumman team did not directly use a linear-theory-based approach in the SSBD design, theirs was a pure CFD approach [26]. However, the application of the UCB area slicing routine and the ARAP propagation code closely reproduced the N-wave and flattop signatures obtained during the flight tests. The added benefit of the UCB approach is that the equivalent-body area distribution, $F(y)$, and near-field overpressure signatures allow shocks to be directly traced to geometric features such as the canopy, inlet, etc. This provides a powerful preliminary design tool whether it is then applied to the UCB optimization schemes or to a CFD-based scheme. (Note that the UCB optimization scheme is also CFD-based, but the optimization iterations use the linear-theory-based F-function).

Selected results from Ref. [6] illustrate the power of the current optimization scheme to directly morph the aircraft shape. A relaxation of the geometric constraints on the F5-E and SSBD geometries generated bulbous and shovel-nosed shapes that minimize ISPR. This again is clear

verification of the result, emphasized by Seebass [27] and Darden [12], that a blunt-nosed aircraft generates a lower ISPR than a more needle-nosed shape.

A study with a geometrically simple aircraft with analytical representations for volume and lift is proposed to develop a more specific application of local *F*-function lobe balancing to focus on the components that drive the formation of intermediate shock waves. The goal will then be to modify the current global algorithm for more targeted aircraft shaping that minimizes the coalescence of the major intermediate shocks with the bow and tail shocks.

6 Acknowledgement

The authors acknowledge the contributions of Hwapyong Ko, University of Colorado Charbel, and Joe Pawlowski and David Graham of the Northrup Grumman Corp.

7 References

1. Seebass, A. R. and Argrow, B. M., "Sonic Boom Minimization Revisited," AIAA Paper 98-2956, 29th AIAA Fluid Dynamics Conference, Albuquerque, NM, Jun. 15-18, 1998.
2. Whitham, G. B, "The Flow Pattern of a Supersonic Projectile." *Communications on Pure and Applied Mathematics*, Vol. 5, 1952, pp. 301-348.
3. Argrow, B, Farhat, C., Maute, K., and Nikbay, M., "Linear-Theory-Based Shape Optimization for Sonic Boom Minimization," Proceedings of the IUTAM Symposium Transsonnicum IV, Göttingen, Germany, Sep. 2002.
4. Farhat, C., Argrow, B., Nikbay, M., and Maute, K., "Shape Optimization with *F*-Function Balancing for Reducing the Sonic Boom Initial Shock Pressure Rise," *International Journal of Aerocoustics*, Vol. 3, No. 4, 2004, pp. 361-377.
5. Farhat, C., Maute, K., Argrow, B., and Nikbay, M., "A Shape Optimization Methodology for Reducing the Sonic Boom Initial Shock Pressure Rise," *AIAA Journal* 45, 5, 2007, pp. 1007-1018.
6. Maute, K., Farhat, C., Argrow, B., and Nikbay, M., "Sonic Boom Mitigation Via Shape Optimization using an Adjoint Methd and Application to a Supersonic Fighter Aircraft," To appear in *European Journal of Computational Mechanics*, 2008.
7. Kane, E. J., "Some Effects of the Atmosphere on Sonic Boom," *Sonic Boom Research*, A. R. Seebass, ed., NASA SP-147, 1967, pp. 49-63
8. Garrick, I. E., "Atmospheric Effects on the Sonic Boom," *Second Conference on Sonic Boom Research*, I. R. Schwartz, ed., NASA SP-180, 1968, pp. 3-17.
9. Koegler, R. K., "Sonic Boom Analysis," AIAA Paper No. 66-941, 1966.
10. Koegler, R. K., "Possible Means of Reducing Sonic Booms and Effects Through Shock Decay Phenomena and Some Comments on Aural Response," *Sonic Boom Research*, A. R. Seebass, ed., NASA SP-147, 1967, pp. 95-102.
11. Hayes, W. D. and Haefeli, R. C., "The ARAP Sonic Boom Program, *Sonic Boom Workshop*, Ed. I. A. Schwartz, NASA SP-180, 1968, 151-158.

12. Darden, C. M., "Sonic Boom Minimization with Nose-Bluntness Relaxation," NASA TN 1348, 1979.

13. Darden, C. M., "Sonic Boom Theory: Its Status in Prediction and Minimization," *Journal of Aircraft*, Vol. 129, No. 6, pp. 569-576, 1977.

14. Hayes W. D., "Brief Review of Basic Theory," *Sonic Boom Research*, A. R. Seebass Ed., NASA SP-147, 1967, pp. 3-7.

15. Ferri, A. "Brief Remarks on Sonic Boom Reduction," *Sonic Boom Research*, A.R. Seebass, Ed., NASA SP-147, 1967, p. 107.

16. Resler, E. L., Jr. "Reduction of Sonic Boom attributed to Lift," *Second Conference on Sonic Boom Research*, Ed. I. R. Schwartz, NASA SP-180, 1968, pp. 99-106.

17. Seebass, A. R., "General Remarks on Sonic Boom, "Reduction of Sonic Boom attributed to Lift," *Second Conference on Sonic Boom Research*, Ed. A.R. Seebass., NASA SP-180, 1968, pp. 175-179.

18. Miller, D. S. and Carlson, H. W. "A Study of the Application of Heat or Force-Fields to the Sonic-Boom Minimization Problem." NASA TN-5582, 1969.

19. Miller, D. S. "Status of Research on Boom Minimization Through Airstream Alteration," *Third Conference on Sonic Boom Research*, Ed. I. R. Schwartz, NASA SP-255, 1970, pp. 325-350.

20. Swigart, R. J. "An Experimental Study of the Validity of the Heat-Field Concept for Sonic-Boom Alleviation." NASA CR-2381, 1974.

21. Shneider, M. N., Macheret, S. O., Zaidi, S. H., Girgis, I. G., Raizer, Yu. P., and Miles, R. B., "Steady and Unsteady Supersonic Flow Control with Energy Addition," AIAA Paper 2003-3862, Plasmadynamics and Lasers Conf., Jun. 2003.

22. Marconi, F., Bowersox, R. D. W., and Schetz, J. A., "Sonic Boom Alleviation Using Keel Configurations," J. Aircraft, 40, No. 2, 2003, pp. 363-369.

23. Zucrow, M. J. and Hoffman, J D., *Gas Dynamics Vol. 1*, John Wiley and Sons, New York, 1976.

24. Incropera, F. P. and DeWitt, D. P., *Fundamentals of Heat and Mass Transfer, 4th Ed.*, John Wiley and Sons, New York, 1996, pp. 435-439, 839.

25. Mattingly, J., Heiser, W. H., and Pratt, D. T., *Aircraft Engine Design, 2nd Ed.*, AIAA Education Series, 2002, http://www.aircraftenginedesign.com.

26. Pawlowski, J. W., Graham, D. H., Boccadoro, C. H., Coen, P. G., and Maglieri, D. J., "Origins and Overview of the Shaped Sonic Boom Demonstration Program," AIAA Paper 2005-5, 43rd AIAA Aerospace Sciences Meeting and Exhibit, Jan., 2005.

27. Seebass, A. R., "Sonic Boom Theory," *Journal of Aircraft*, Vol. 6, No. 3, 1969, pp. 177-184.

28. McLean, E. F., "Some Nonasymptotic Effects on the Sonic Boom of Large Airplanes," NASA TN D-2877, 1965.

29. Runyan, H. L. and Henderson, H. R., "Evaluation of Certain Minimum Boom Concepts," NASA SP-180, 1968, pp. 45-55.

30. Mack, R. J. and Darden, C. M., "Wind Tunnel Investigation of the Validity of a Sonic-Boom-Minimization Concept," NASA TP 1421, 1979.

31. Siegelman, D., "Sonic Boom Minimization Schemes." *Journal of Aircraft*, Vol. 7, No. 3, 1970, pp. 280–281.

32. Ferri, A. and Ismail, A., "Report on Sonic Boom Studies: Part I—Analysis of Configurations," *Second Conference on Sonic Boom Research*, Ed. I. R. Schwartz, NASA SP-180, 1968, pp. 73-88.

33. Morris, J., "An Investigation of Lifting Effects on the Intensity of Sonic Booms," *Journal of the Royal Aeronautical Society*, 1960, pp. 610-616.

34. Gottlieb, J. J. and Ritzel, D. V., "Analytical Study of Sonic Boom from Supersonic Projectiles," *Prog. Aerospace Sci.*, Vol. 25, pp. 131-188, 1988.